



Analysis of likelihood of lower head failure and ex-vessel fuel coolant interaction energetics for AP1000

H. Esmaili, M. Khatib-Rahbar*

Energy Research Inc., P.O. Box 2034, Rockville, MD 20847-2034, USA

Received 29 August 2004; accepted 3 February 2005

Abstract

A one-dimensional model is formulated to assess the thermal response of the Westinghouse Advanced Plant (AP1000) lower head based on two bounding melt configurations. Melt Configuration I involves a stratified light metallic layer on top of a molten ceramic pool, and melt Configuration II represents the conditions that an additional heavy metal layer forms below the ceramic pool. The approach consists of the specification of initial conditions; determination of the mode, the size and the location of lower head failure based on heat transfer analyses; computer simulation of the fuel coolant interaction processes; and finally, an examination of the impact of the uncertainties in the initial conditions and the model parameters on the fuel coolant interaction energetics through a series of sensitivity calculations. The results of the calculations for melt Configuration I show that the heat flux remains below critical heat flux (CHF) in the molten oxide pool, but the heat flux in the light metal layer could exceed CHF because of the focusing effect associated with presence of the thin metallic layers. The thin metallic layers are associated with smaller quantities of the molten oxide in the lower plenum following the initial relocation into the lower head. The calculations show that the lower head failure probability due to the focusing effect of the stratified metal layer ranges from ~ 0.04 to ~ 0.30 . On the other hand, the thermal failure of the lower head at the bottom location for melt Configuration II is assessed to be highly unlikely. Based on the in-vessel retention analysis, the base case for the ex-vessel fuel coolant interaction (FCI) is assumed to involve a side failure of the vessel involving a metallic pour into the cavity water. The FCI sensitivity calculations intended to assess the implications of the uncertainties in initial conditions and the FCI modeling parameters show that the FCI loads range from a few MPa to upward of 1000 MPa (maximum pool pressure) with corresponding impulse loads ranging from a few kPa s to a few hundred kPa s.

© 2005 Elsevier B.V. All rights reserved.

1. Introduction

The physical processes involved in the late in-vessel phase of severe accidents in light water reactors (LWRs) are very complex and remain uncertain. Under postulated severe accident conditions, large quantities

* Corresponding author. Tel.: +1 301 881 0866;
fax: +1 301 881 0867.

E-mail address: mkr@eri-world.com (M. Khatib-Rahbar).

Nomenclature

$A_{h,b}$	heat transfer area between the heavy metal layer and the vessel (m^2)
$A_{h,t}$	heat transfer area between the heavy metal layer and the lower crust (m^2)
$A_{l,b}$	heat transfer area of between the upper crust of the ceramic pool and the light metallic layer (m^2)
$A_{l,t}$	heat transfer area between the light metallic layer and the reactor internal atmosphere (m^2)
$A_{l,w}$	heat transfer area between the light metallic layer and the adjacent reactor vessel (m^2)
$A_{o,b}$	heat transfer area between the oxide pool and the bottom crust of the ceramic pool (m^2)
$A_{o,t}$	heat transfer area between the oxide pool and the top crust (m^2)
$A_{o,w}$	heat transfer area between the oxide pool and the crust layer adjacent to the vessel wall (m^2)
A_s	total surface area of all core internal structures exposed to the molten pool (m^2)
$A_{w,i}$	heat transfer area between the vessel wall and the crust of the oxide pool adjacent to it (m^2)
H	height of the molten layer (m)
h_{boil}	coefficient for nucleate pool boiling heat transfer ($W/m^2 K^3$)
$h_{l,b}$	heat transfer coefficient at the light metallic layer-lower oxide crust juncture ($W/m^2 K$)
$h_{l,t}$	heat transfer coefficient at the top surface of the light metallic layer ($W/m^2 K$)
$h_{l,w}$	heat transfer coefficient at the light metal layer, vessel wall juncture ($W/m^2 K$)
$h_{o,b}$	heat transfer coefficient at the oxide pool-lower crust juncture ($W/m^2 K$)
$h_{o,t}$	heat transfer coefficient at the oxide pool-upper crust juncture ($W/m^2 K$)
$h_{o,w}$	heat transfer coefficient at the oxide pool-wall crust juncture ($W/m^2 K$)

k_c	thermal conductivity of the crust ($W/m K$)
k_w	thermal conductivity of the vessel wall ($W/m K$)
Nu	Nusselt number
Q_c'''	volumetric heat generation rate in the oxide crust (W/m^3)
Q_h'''	volumetric heat generation rate in the heavy metal layer (W/m^3)
Q_l'''	volumetric heat generation rate in the light metal layer (W/m^3)
Q_o'''	volumetric heat generation rate in the oxide pool (W/m^3)
q_{CHF}''	critical heat flux (CHF) (W/m^2)
$q_{h,b}''$	heat flux from the heavy metal layer to the bottom of the vessel (W/m^2)
$q_{h,t}''$	heat flux from the lower oxide pool crust into the heavy metal layer (W/m^2)
$q_{l,b}''$	heat flux from the top oxide pool crust into the top light metal layer (W/m^2)
$q_{l,t}''$	heat flux from the top light metal layer into the internal atmosphere of the reactor (W/m^2)
$q_{l,w}''$	heat flux from the top light metal layer into the vessel wall (W/m^2)
$q_{o,b}''$	heat flux from the oxide pool into the lower crust (W/m^2)
$q_{o,t}''$	heat flux from the oxide pool into the top crust (W/m^2)
$q_{o,w}''$	heat flux from the oxide pool into the crust adjacent to the vessel wall (W/m^2)
$q_{w,i}''$	heat flux from the oxide pool crust that exists adjacent to the vessel wall into the vessel wall (W/m^2)
$q_{w,o}''$	heat flux from the vessel wall into the cavity water (W/m^2)
R	lower head radius (m)
Ra	Rayleigh number (based on internal heat generation)
T_b^l	bulk temperature of the light metal layer (K)
$T_{h,t}$	temperature at the heavy metal layer-bottom crust juncture (K)

$T_{l,t}$	temperature at the light metal layer-atmosphere interface (K)
$T_{l,b}$	temperature at the light metal layer-lower oxide crust juncture (K)
T_m^o	melting temperature of the oxide pool (K)
T_m^v	melting temperature of vessel wall (K)
T_{max}^o	maximum temperature of the oxide pool (K)
T_s	temperature of internal structures (K)
T_{sat}	saturation temperature of cavity water (K)
$T_{w,i}$	inside vessel wall temperature (K)
$T_{w,o}$	outside vessel wall temperature (K)
$V_{c,l}$	volume of the lower oxide crust (m^3)
$V_{c,u}$	volume of the upper oxide crust (m^3)
$V_{c,w}$	volume of the oxide crust that exists adjacent to the vessel wall (m^3)
V_h	volume of the heavy metal layer (m^3)
V_l	volume of the light metal layer (m^3)
V_o	volume of the oxide pool (m^3)

Greek symbols

δ_s	vessel wall thickness (m)
δ_c	oxide crust thickness (m) (further indexed by u, l and w for upper, lower and wall)
ε_t	emissivity at the light metal layer-atmosphere interface
ε_s	emissivity of the core internal structures
σ	Stefan-Boltzmann constant ($5.672 \times 10^{-8} \text{ W/m}^2 \text{ K}^4$)

of molten core material may relocate to the lower plenum of the reactor pressure vessel (RPV) where it interacts with water, lower plenum and RPV structures. The heat transfer from the molten debris causes evaporation of any remaining water and heat-up of the lower plenum and vessel structures. If the reactor cavity is flooded before melt relocation into the lower plenum, the vessel wall would be initially cool and the outer vessel temperature would remain close to the cavity water saturation temperature. Nucleate pool boiling of the cavity water is an efficient mechanism for heat removal from the molten debris in the lower plenum.

Provided that adequate heat removal could not be achieved, and if the local heat flux at the vessel wall were to exceed the critical heat flux, vessel failure would be expected.

Following the structural failure of the lower head, the molten core debris will pour into the reactor cavity where the potential for energetic fuel-coolant interaction (FCI) with cavity water exists. This energetic FCI is initiated by transfer of energy from the hot liquid (fuel) to the colder liquid (coolant) during liquid-liquid contact resulting in rapid steam generation that could lead to a high local pressure. The dynamic loads on the cavity wall and the RPV structures could potentially lead to the failure of the cavity wall and/or subjecting the primary system piping connected to the steam generators and the main steam lines penetrating the containment boundary, to severe mechanical loads that could challenge the containment integrity.

The core debris attack on the RPV lower head and the in-vessel retention (IVR) of molten core debris inside RPV lower head through external cooling by cavity water has been the subject of numerous numerical and experimental investigations as exemplified by Turland and Morgan (1983), Park and Dhir (1991), O'Brien and Hawkes (1991), Henry and Fauske (1993), Turland (1994), Theofanous et al. (1994a,b), Khatib-Rahbar et al. (1996), Esmaili et al. (1996), Asfia and Dhir (1996), Theofanous et al. (1996), Rempe et al. (1997), Kymfilfinen et al. (1997), Theofanous and Angelini (2000), Sehgal et al. (2003) and Seiler et al. (2003), which include one-, and two-dimensional calculations, measurements of natural convection heat transfer in simulated molten pool configurations, and measurements of critical heat flux applicable to boiling on the external surface of the RPV lower head.

In one of the earliest studies, a one-dimensional model was proposed by O'Brien and Hawkes (1991) to study the thermal response of the RPV lower head following core relocation to the lower plenum. The model allowed for the spherical geometry of the lower head with convective heat transfer in the molten pool. A similar one-dimensional model was developed by Esmaili et al. (1996). The capability of the external cooling of the RPV lower head to prevent failure considering the presence of the RPV insulation was studied by Henry and Fauske (1993). The analysis of the thermal response of the lower head was very simple assuming a partitioning of the heat transfer in the molten ceramic pool and

one-dimensional conduction in the vessel wall. The focus of the analysis (Henry and Fauske, 1993) was to assess the water inflow through the insulation and the two-phase heat removal in the gap between the insulation and the vessel wall.

The mathematical models used for the thermal response of the lower head have included both one-dimensional (O'Brien and Hawkes, 1991; Esmaili et al., 1996; Theofanous et al., 1996; Rempe et al., 1997) and two-dimensional models (Park and Dhir, 1991; Khatib-Rahbar et al., 1996). A comparison of the one-dimensional and two-dimensional models by Esmaili et al. (1996) showed that a one-dimensional heat conduction model of the lower head performed adequately and the second order effects using a two-dimensional model were found to be small considering the uncertainties associated with the late phase in-vessel melt progression.

The study of the in-vessel retention under externally cooled conditions requires closure relations for heat transfer in the molten ceramic and metallic regions. Allison et al. (1994) provided a detailed review of the heat transfer correlations for volumetrically heated pools. This review (Allison et al., 1994) included experimental and numerical studies that had been reported in the literature for flat surfaces and curved configurations. A summary of the various heat transfer correlations for the ceramic pool and the stratified light molten metallic layer is also provided by Theofanous et al. (1996) and Rempe et al. (1997). In the present study, references to these heat transfer correlations have been made where appropriate.

If the RPV lower head could not be cooled, the failure of the lower head is a certainty, resulting in the relocation of molten core debris into the cavity water, potentially leading to an energetic fuel coolant interaction.

The modeling of fuel coolant interactions remains difficult and analysis results are also subject to large uncertainties. Examples of one- and two-dimensional FCI models that have been developed over the last twenty years include the TEXAS code (Young, 1982) and the PM-ALPHA/ESPROSE (Yuen and Theofanous, 1995; Theofanous and Yuen, 1995) computer codes. The FCI models are evolving as additional experimental data become available. In addition to the uncertainties inherent in modeling FCI processes, other major uncertainties that affect the explosion energetic include

the water pool sub-cooling, the lower head failure size and location, and the melt composition and temperature.

The main objective of the present paper is to present a simple mechanistic model based on the existing constitutive relations, originally developed for AP600 (Khatib-Rahbar et al., 1996; Esmaili et al., 1996) that is used together with a synthesis of severe core damage phenomenology, to arrive at a likelihood of vessel failure for AP1000 (Esmaili and Khatib-Rahbar, 2004). In addition, the present study provides an assessment of the ex-vessel fuel coolant interaction energetics following a similar approach that was used for AP600 (Khatib-Rahbar et al., 1996).

2. Mathematical model for IVR analysis

The model is based on a conceptual representation of two melt configurations shown in Fig. 1. The melt Configuration I is assumed to represent a two-layer melt pool with a light metallic layer of Fe–Zr on top of a ceramic pool of $\text{UO}_2\text{--ZrO}_2$ as shown in Fig. 1a. On the other hand, the melt Configuration II is assumed to represent a stratified molten pool consisting of a dense metallic layer of Zr–U–Fe (in the bottom), a ceramic layer of $\text{UO}_2\text{--ZrO}_2$ (in the middle), and a light metallic layer of Fe–Zr (on top) as shown in Fig. 1b. The ceramic layer does not contain any metals, and the top metallic layer is assumed to contain no metallic uranium. It is recognized that other configurations of the molten pool can be also envisioned (Rempe et al., 1997); however, in terms of the potential implications on the lower head integrity, the present three-layer configuration is considered to be adequate.

2.1. Governing equations

The conservation of energy equation can be written for each layer subject to the following limitations:

1. The heat generation in the vessel wall is negligible;
2. The radiation heat transfer from the light metal layer top surface is not sufficient to form a metallic crust; and
3. The potential impacts of materials interactions (i.e., heat of mixing and autocatalytic effects) are not considered.

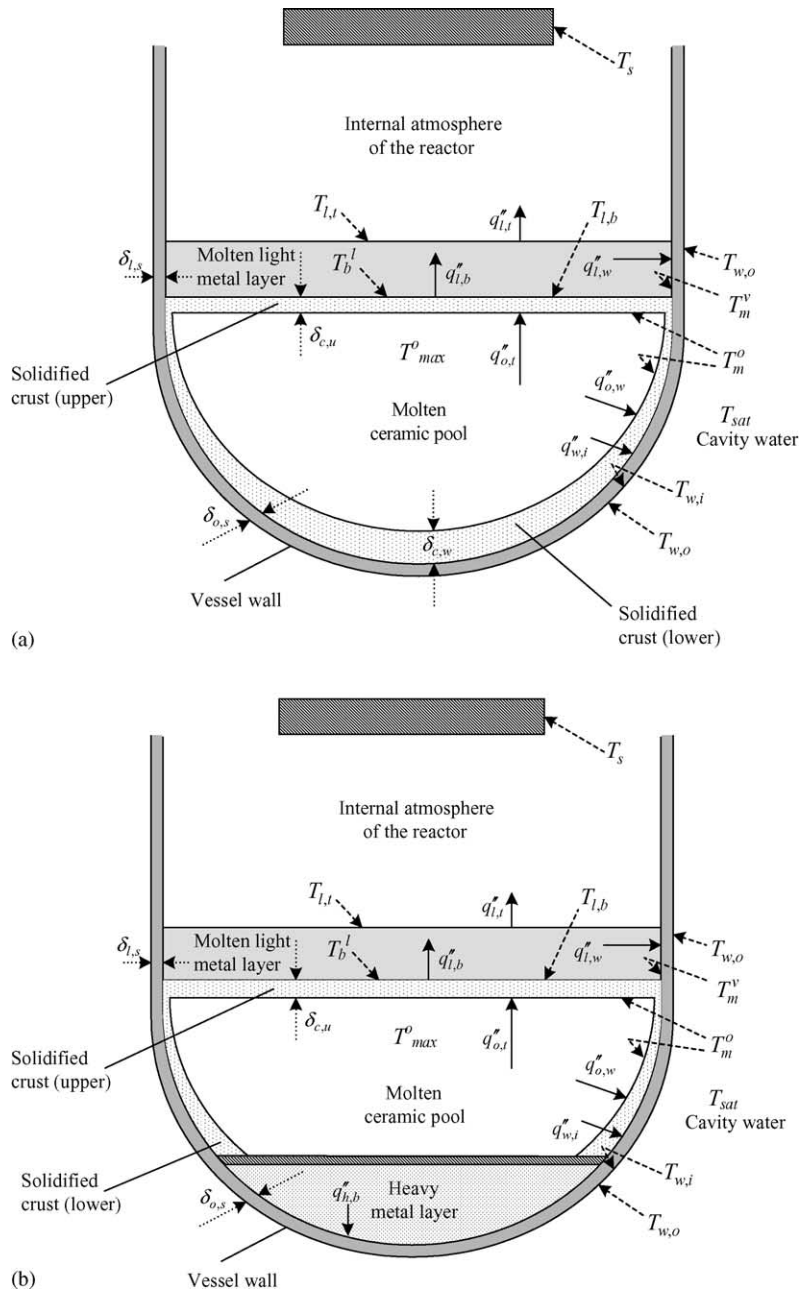


Fig. 1. (a) Schematic of the melt pool Configuration I in the lower head (two layers); (b) schematic of the melt pool Configuration II in the lower head (three layers).

Top light metal layer

$$Q_1''' V_1 + q_{1,b}'' A_{1,b} = q_{1,t}'' A_{1,t} + q_{1,w}'' A_{1,w} \quad (1)$$

Middle ceramic (oxide) pool

$$Q_o''' V_o = q_{o,t}'' A_{o,t} + q_{o,w}'' A_{o,w} + q_{o,b}'' A_{o,b} \quad (2)$$

$$q_{1,b}'' A_{1,b} = Q_c''' V_{c,u} + q_{o,t}'' A_{o,t} \quad (3)$$

$$q_{w,i}'' A_{w,i} = q_{o,w}'' A_{o,w} + Q_c''' V_{c,w} \quad (4)$$

$$q_{h,t}'' A_{h,t} = q_{o,b}'' A_{o,b} + Q_c''' V_{c,l} \quad (5)$$

Bottom heavy metal layer

$$Q_h''' V_h + q_{h,t}'' A_{h,t} = q_{h,b}'' A_{h,b} \quad (6)$$

2.2. Heat transfer in molten layers

Assuming there is no metallic crust because of high heat transfer rates in the metal layer, the heat flux at the upper surface of the light metal layer (on top of the ceramic layer) can be calculated using:

$$q_{1,t}'' = h_{1,t}(T_b^1 - T_{1,t}) \quad (7)$$

The heat loss from the top surface of the light metallic layer, by radiation, to the other structures in the reactor pressure vessel is approximated by the following equation:

$$q_{1,t}'' = \frac{\sigma [T_{1,t}^4 - T_s^4]}{\left[\frac{1}{\varepsilon_t} + \frac{1-\varepsilon_s}{\varepsilon_s} \frac{A_{1,t}}{A_s} \right]} \quad (8)$$

The heat flux from the light metallic layer to the vessel wall and through the sidewall can be expressed as:

$$q_{1,w}'' = h_{1,w}(T_b^1 - T_m^v) \quad (9)$$

$$q_{1,w}'' = \frac{k_w}{\delta_s}(T_m^v - T_{w,o}) \quad (10)$$

$$q_{1,w}'' = h_{boil}(T_{w,o} - T_{sat}) \quad (11)$$

The heat flux from the top oxide crust to the light metallic layer can be estimated using:

$$q_{1,b}'' = h_{1,b}(T_{1,b} - T_b^1) \quad (12)$$

The heat flux from the ceramic pool to the surrounding crust that is in contact with the lower head can be

written as:

$$q_{o,w}'' = h_{o,w}(T_{max}^o - T_m^o) \quad (13)$$

The heat flux at the inner and the outer boundaries of the ceramic crust can be expressed as:

$$q_{o,w}'' = \frac{k_c}{\delta_{c,w}}(T_m^o - T_{w,i}) - \frac{Q_c''' \delta_{c,w}}{2} \quad (14)$$

$$q_{w,i}'' = \frac{k_c}{\delta_{c,w}}(T_m^o - T_{w,i}) + \frac{Q_c''' \delta_{c,w}}{2} \quad (15)$$

Since it is assumed that the heat generation in the vessel wall can be neglected, the heat flux by conduction through the lower head can be expressed by:

$$q_{w,i}'' = \frac{k_w}{\delta_s}(T_{w,i} - T_{w,o}) \quad (16)$$

$$q_{w,i}'' = q_{w,o}'' = h_{boil}(T_{w,o} - T_{sat}) \quad (17)$$

The heat flux to the light metal layer through the upper ceramic crust is estimated using:

$$q_{o,t}'' = h_{o,t}(T_{max}^o - T_m^o) \quad (18)$$

$$q_{o,t}'' = \frac{k_c}{\delta_{c,u}}(T_m^o - T_b^1) - \frac{Q_c''' \delta_{c,u}}{2} \quad (19)$$

$$q_{1,b}'' = \frac{k_c}{\delta_{c,u}}(T_m^o - T_b^1) + \frac{Q_c''' \delta_{c,u}}{2} \quad (20)$$

Similarly, the heat flux through the lower ceramic crust is estimated using:

$$q_{o,b}'' = h_{o,b}(T_{max}^o - T_m^o) \quad (21)$$

$$q_{o,b}'' = \frac{k_c}{\delta_{c,l}}(T_m^o - T_{h,t}) - \frac{Q_c''' \delta_{c,l}}{2} \quad (22)$$

$$q_{h,t}'' = \frac{k_c}{\delta_{c,l}}(T_m^o - T_{h,t}) + \frac{Q_c''' \delta_{c,l}}{2} \quad (23)$$

The heat flux characteristic in the heavy metallic layer is complicated. The top surface of the heavy metallic layer is hot because it is in contact with the molten ceramic pool, and the bottom surface of the heavy metallic layer is cool due to nucleate boiling on the outside surface of the lower head. In this melt configuration, the temperature gradient is governed by the magnitude of the internal heat generation, the temperature of the top boundary adjacent to the ceramic layer, and the extent of convective motion that could impact

the degree of thermal stratification that is expected to develop. The denser cooler fluid will sink to the bottom of the layer, and in the absence of significant natural convection, the heat transfer in this stratified configuration is dominated by conduction of heat through the layer. The presence of volumetric heating in the heavy metallic layer can further complicate the heat transfer process. To envision the thermal response, consider a slab with internal heat generation, maintained at a higher temperature on the top surface, and lower temperature at the bottom surface. For this case, the maximum temperature occurs at a distance from the top surface inside the slab. In the limit, the location of the maximum temperature can be at the hot surface where the heat flux is zero. Under these conditions, the hot surface is effectively insulated and the heat generated in the layer would have to be transferred to the cold surface. If the maximum temperature is inside the slab, then the heat is transferred away from the layer to both the top hot surface and the bottom cool surface. An analysis of the heat transfer mechanism and interaction with the ceramic layer is presented by Scobel (2003). In the present paper, it is conservatively assumed that: (i) heat transfer to the vessel wall involves the entire decay heat in the heavy metallic layer; and (ii) the heat transfer at the interface from the heavy metallic layer to the ceramic layer is zero (i.e., an insulated top surface). Therefore, using Eq. (6), the heat flux to the bottom surface of the heavy metallic layer is estimated as follows:

$$q''_{h,b} = \frac{Q'''_h V_h}{A_{h,b}} \tag{24}$$

Furthermore, the heat flux in the vessel wall is given by:

$$q''_{h,b} = \frac{k_w}{\delta_s} (T_{w,i} - T_{w,o}) \tag{25}$$

Empirical natural convection heat transfer correlations are presented in Table 1. The experimental range of these correlations are listed in Table 2, which cover the expected Rayleigh number and Prandtl number regimes in the lower head.

In addition, the boiling heat transfer correlation in Eq. (17) uses the Rohsenow pool boiling correlation (Rohsenow, 1952).

The partitioning of the decay heat between the ceramic and the heavy metallic layers is calculated using

Table 1
Heat transfer correlations used in the present model

Region	Top surface	Bottom surface	Side wall	Angular variation
Metallic layer	Globe and Dropkin (1959) $Nu_t = 0.069 Ra_t^{0.333} Pr_t^{0.074}$	Globe and Dropkin (1959) $Nu_b = 0.069 Ra_b^{0.333} Pr_b^{0.074}$	Churchill and Chu (1975), $Nu_{t,w} = \left[0.825 + \left(\frac{0.387 Ra_t^{1/6}}{1 + (0.492/Pr_t)^{9/16}} \right)^2 \right]^{8/27}$	
Ceramic pool	Kulaeki and Emara (1975) $Nu_u = 0.345 (Ra_{qu})^{0.226}$	Mayinger et al. (1976) $Nu_d = 0.55 (Ra_{qd})^{0.2}$		Park and Dhir (1992), $h_d(\theta) = \bar{h}_d (b_1 \sin^2 \theta + b_2)$, $b_1 = \frac{9.12(1 - \cos \theta_0)}{8 - 9 \cos \theta_0 + \cos 3\theta_0}$, $b_2 = 0.24$

Table 2
Ranges of applicability of the correlations

Model	Heat transfer correlation	Range of applicability	
		Ra	Pr
Top metal layer	Globe and Dropkin (1959)	3×10^5 to 7×10^9	0.02–8750
	Churchill and Chu (1975)	$0.1-10^{12}$	All
Ceramic pool	Kulacki and Emara (1975)	2×10^4 to 4.4×10^{12}	7
	Mayinger et al. (1976)	7×10^6 to 5×10^{14}	0.5

a simple approach that is based on the mass fraction of U in the respective layers, that is:

$$Q_h''' + Q_o''' V_o = P_{\text{decay}} - \text{tot}$$

$$\frac{Q_h''' V_h}{Q_o''' V_o} = \frac{m_U(270/238)}{m_{\text{UO}_2}} \quad (26)$$

where m_U is the mass of uranium in the bottom (heavy) metallic layer, and m_{UO_2} the mass of UO_2 in the ceramic layer.

Another approach (Scobel, 2003) would be to partition the decay heat into the bottom heavy metal layer based on the equivalent volume of the material that has reacted to produce the uranium metal:

$$\frac{Q_h'''}{Q_o'''} = \frac{m_U(270/238)}{\rho_o V_h} \quad (27)$$

The impact of heat generation in the upper metallic layer is assessed as part of a sensitivity study that is discussed later. For this case, the fraction of decay heat in the metal layer is estimated as (Rempe et al., 1997):

$$f_{\text{metal}} = (1 - f_{\text{ox-Zr}})[f_{\text{group 4}} + f_{\text{Zr and Nb}}] + f_{\text{group 6}} \quad (28a)$$

$$f_{\text{Zr and Nb}} = M_{\text{Zr and Nb}} t_r + B_{\text{Zr and Nb}} \quad (28b)$$

$$f_{\text{group 6}} = M_{\text{group 6}} t_r + B_{\text{group 6}} \quad (28c)$$

$$f_{\text{group 4}} = M_{\text{group 4}} t_r + B_{\text{group 4}} \quad (28d)$$

where t_r is the time of core release, $f_{\text{ox-Zr}}$ the fraction of Zr oxidized, and the coefficients are listed in Table 3 (Rempe et al., 1997).

The system of Eq. (1) through Eq. (25) is solved using a non-linear Newton–Raphson method that accounts for temperature dependence of the viscosity. The material properties are calculated using the approach as proposed by Rempe et al. (1997).

2.3. Critical heat flux

The critical heat flux correlation is given as (Esmaili and Khatib-Rahbar, 2004):

$$q_{\text{CHF}}'' = 1.44 \times (A + B\theta + C\theta^2 + D\theta^3 + E\theta^4) \quad (29)$$

where the coefficients A through E are based on experimental results (W/m^2) for AP600 (Theofanous et al., 1996), and θ the lower head angle in degrees. The factor 1.44 is used in the present paper to account for the higher values of the critical heat flux for the latest lower head configuration design (Configuration V) in AP1000. A comparison of this approach to the latest data for Configuration V in AP1000 (Dinh et al., 2003) shows (Esmaili and Khatib-Rahbar, 2004) that the factor of 1.44 provides a good estimate for the critical heat flux up to an angle of about 70° , but it overestimates the critical heat flux near the top. The reason for the critical heat flux not consistently increasing near the top requires further investigation (Dinh et al., 2003).

2.4. Model verification

The present model has been benchmarked against the results of Theofanous et al. (1996) and Rempe et al. (1997) as discussed by Esmaili and Khatib-Rahbar (2004). As part of this benchmarking exercise, two calculations were performed. In the first calculation, the

Table 3
Coefficient used in Eqs. (28a)–(28d) (Rempe et al., 1997)

Parameter	$0 \leq t_r < 18000$ s	$18000 \leq t_r < 28880$ s
$B_{\text{group 4}}$	0.0572	0.0334
$B_{\text{group 6}}$	0.0688	0.0828
$B_{\text{Zr and Nb}}$	0.1068	0.1326
$M_{\text{group 4}}$	$-1.473\text{E}-6$	$-1.502\text{E}-7$
$M_{\text{group 6}}$	$+1.236\text{E}-6$	$+4.572\text{E}-7$
$M_{\text{Zr and Nb}}$	$+2.154\text{E}-6$	$+7.197\text{E}-7$

heat transfer correlations were assumed to be the same as those by Theofanous et al. (1996). In the second calculation, the heat transfer correlations were changed to those of Table 1. The initial conditions for the benchmarking calculation were taken directly from Rempe et al. (1997). In general, the results of the calculations showed good agreement (Esmaili and Khatib-Rahbar, 2004) with those of Theofanous et al. (1996) and Rempe et al. (1997), with differences attributed to the lack of documented information on some of the initial conditions used in the analyses as also discussed by Rempe et al. (1997).

3. Specification of initial conditions for IVR analysis

The uncertainties associated with the initial conditions include the decay power, fraction of Zr oxidation, mass of UO_2 relocation to the lower plenum, and the amount of steel in the lower plenum debris, considering the two bounding melt Configurations I and II.

The mass and composition of debris in the lower plenum after core relocation is dependent on the accident scenario. However, there are significant uncertainties with late phase melt progression. In the present assessment, the scenarios of interest involve full depressurization of the reactor coolant system (RCS). The quantification of the initial and boundary conditions is mainly based on the results of plant-specific MELCOR and MAAP calculations in AP1000 for depressurized scenarios (Zavisca et al., 2003; Yuan et al., 2003) and insights from the SCDAP/RELAP5 calculations (Khatib-Rahbar et al., 1996; Rempe et al., 1997). The uncertainty distributions are developed for the proposed melt Configuration I only. For melt Configuration II, only sensitivity calculations are performed.

The decay heat in the ceramic pool plays an important role in the total heat flux from the debris to the vessel wall and the molten metal layers. Therefore, the quantification of the decay power in the ceramic pool is very important. It should be noted that in the melt Configuration I, the decay energy is assumed to reside in the ceramic pool by default. For the melt Configuration II, the decay power is partitioned between the ceramic pool and the bottom (heavy) metallic layer. According to plant-specific MELCOR calculations (Zavisca et al., 2003), core relocation to the lower plenum occurs be-

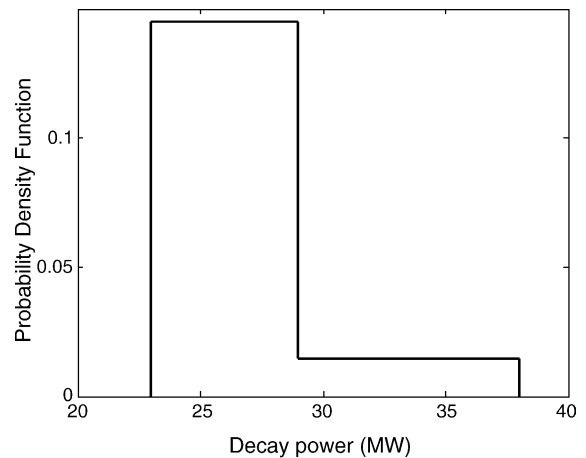


Fig. 2. Distribution of decay power.

tween 2.6 and 3.7 h depending on the scenario. At the time of core relocation to the lower plenum, the whole core decay heat ranges from 23 to about 29 MW. This decay power considers the loss of volatile fission products. In the MAAP calculation, the time of core relocation is about 1.7 h, and the total core power is 28.7 MW. For a core relocation time of 6000 s as predicted by MAAP calculation, MELCOR predicts a whole core decay power of 38 MW (Esmaili and Khatib-Rahbar, 2004). Therefore, following the above discussion, the uncertainty distribution for the decay heat as shown in Fig. 2 is proposed.

The results of the MELCOR calculations (Zavisca et al., 2003) show about 50% of the core inventory of Zr is expected to be oxidized prior to significant melt-pool relocation to the lower plenum. In the MAAP calculation, the Zr oxidation fraction was estimated to be about 0.3, which is relatively low. For the high-pressure scenarios considered as part of the NRC direct containment heating (DCH) issue resolution for pressurized water reactors (Pilch et al., 1996), the most probable Zr oxidation fraction was about 0.4, and lowest value was 0.2 with an upper bound was about 0.6. Even though the high-pressure scenario condition is not directly relevant to this study, nevertheless, it is being referenced to show the range of uncertainties that have been considered in recent years and for previous studies. Therefore, following the above considerations, and the results of the MELCOR plant-specific calculations (Zavisca et al., 2003), the most probable range for the present study is between 0.4 and 0.6 as shown in Fig. 3. MELCOR

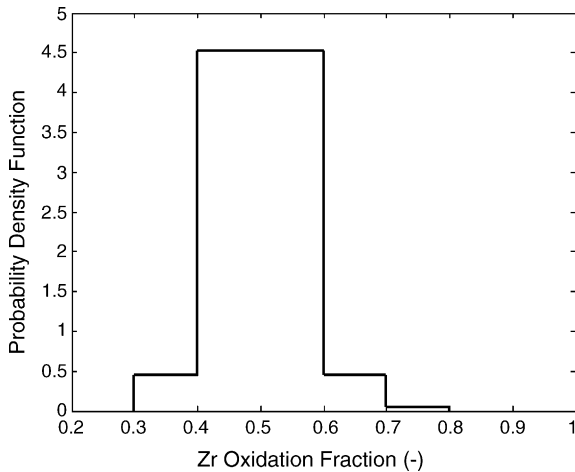


Fig. 3. Distribution of Zr oxidation.

sensitivity calculations (Zavitsca et al., 2003) showed that the Zr oxidation fraction can vary from 0.5 to 0.65. The lower range of 0.3 to 0.4 is considered based on the single MAAP calculation but at a lower probability level of 0.1. The upper bound of the Zr oxidation in this study is assumed to be 0.8. This is mainly due to the fact that even though full-loop natural circulation of steam throughout the primary circuit is expected, nevertheless, metallic blockages impede the extent of Zr oxidation.

In the SCDAP/RELAP5 analysis for AP600 (Khatib-Rahbar et al., 1996), the initial relocation of the core to the lower plenum involved about 50% of the core UO_2 inventory, and the subsequent relocation of an additional 35% of the core UO_2 inventory at about 800 s later. However, this relocation scenario assumed that all relocated debris immediately passed through the perforations in the core support plate. But if the relocated core debris could be retained on the core support plate, additional calculations suggest that the first relocation could last for more than an hour. Clearly, such a case is plausible given inherent uncertainties in late phase melt progression. In the MAAP calculation, the initial crucible contained about 70% of the core UO_2 inventory. Upon failure of the melt crucible/crust, about 50% of the core inventory was predicted to relocate into the lower plenum. However, in the MAAP calculation, the relocation was gradual, and eventually a significant portion of the core relocated to the lower plenum that subsequently resulted in the submergence of the lower

core steel support plate. Therefore, the initial relocation in the MAAP calculation was similar to the SCDAP/RELAP5. This is not to minimize the significant uncertainties in the core relocation, but to emphasize that given the current state of knowledge; an estimate of core relocation can only be made if a wider range of conditions is envisioned. In the AP1000 plant-specific MELCOR calculations (Zavitsca et al., 2003), the initial relocation involved about 80% of core inventory. In the present assessment, it is assumed that a significant portion of the core (~ 70 to 80%) would melt and relocate to the lower plenum, but relocation involving a lower mass of the molten core ($\sim 50\%$) cannot be ruled out. This is true especially in light of the fact that the vessel is cooled with the cavity water flowing through the insulation, and there is potential for cooling of the core barrel (by radiation to the vessel wall, subsequent conduction across the vessel wall and convection/boiling of the cavity water flowing through the insulation). Therefore, it is conceivable that there could be a time window before the occurrence of a second relocation of the ceramic rich molten debris into the lower plenum region.

Using the phenomenological picture just described, the proposed uncertainty distribution of Fig. 4 considers the potential for relocation of a smaller fraction of the core debris into the lower plenum. Note that the upper bound of the uncertainty distribution is not that critical, because as the mass of the ceramic pool increases, it is expected to submerge the core lower support plate resulting in significant addition of molten steel on top

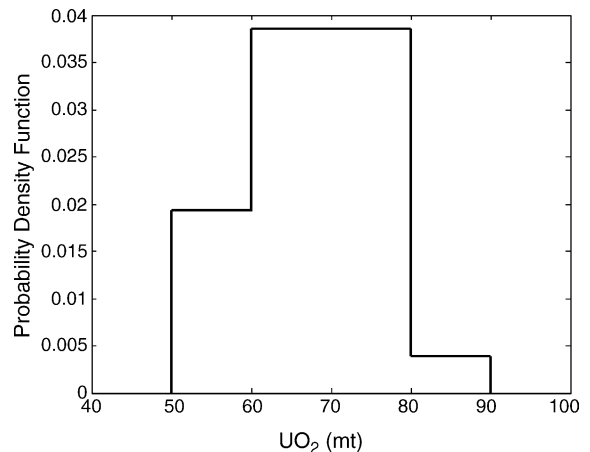


Fig. 4. Distribution of UO_2 in the lower plenum.

of the ceramic pool, thereby mitigating the focusing effect of the thin stratified metallic layer. The mass of ZrO_2 in the ceramic pool is assumed to scale with the mass of fuel relocated to the lower plenum, and the fraction of Zr oxidation.

One of the most important aspects of the in-vessel melt retention is the potential for the formation of a top metallic layer, especially if the layer is thin enough to cause significant focusing effect. In the present assessment, it is assumed that the mass of the steel layer is correlated with the mass of UO_2 in the lower plenum. For a low ceramic pool mass, the lower core support plate would not be submerged and therefore, the amount of steel would be limited. About 60 mt of UO_2 can relocate to the lower plenum without submerging the lower core plate. Under these conditions, the amount of steel in the upper metallic layer is very limited. It is assumed that the lower bound of steel mass is 3 mt that contains only the lower plenum energy absorbers. It is estimated that about 5 mt of core barrel could be molten prior to core relocation. It is assumed that the quantity of steel varies in direct proportion to the mass of UO_2 as shown in Fig. 5. Thus, for the 50–60 mt of UO_2 in the lower plenum, the steel mass can vary between 3 and 8 mt. For higher molten pool mass, the core support plate would be submerged, and therefore, there is a discontinuity in the steel distribution. For this case, it is estimated that the entire lower core support plate would be molten, and significant portion of the core barrel and core shroud would melt and form a molten metallic pool on top of

the ceramic pool. As a best estimate, given that 50% of shroud/barrel melt, the total steel mass is 48 mt, and for the best estimate core UO_2 mass of 60–80 mt, the steel mass is assumed to vary between 40 and 60 mt. For the upper end of the spectrum, and for the higher UO_2 mass, the melt contains the rest of the steel.

Note that metal layer can contain some of the un-oxidized Zr that was previously held-up in the metallic blockages in the lower regions of the core on top of the core support plate.

4. Results of analysis of likelihood of lower head failure

4.1. Probabilistic framework

In the present approach, the uncertainties in accident progression variables, and the model parameters, x_i , are represented by probability density functions, $f(x_i)$, representing the analyst's degree of belief in the expected range of the uncertainty domain.

The uncertainties are propagated through the present model using the latin hypercube sampling (LHS) (Iman and Shortencarier, 1984) technique for the vector of random samples.

The uncertainties in the vessel heat flux loads are determined as the output distributions based on the predictions of the model. The likelihood of vessel failure is dependent on the magnitude of heat flux. If the heat flux to the cavity water at any location exceeds the critical heat flux, RPV lower head failure is assumed.

4.2. Base case (melt Configuration I)

The results of the in-vessel retention are presented in this section. Based on 1000 LHS-generated random samples from the distributions for the material properties, decay heat (Fig. 2), Zr oxidation fraction (Fig. 3), lower plenum ceramic and metal mass (Figs. 4 and 5), and three other parameters listed in Table 4. The mean and standard deviation values in Table 4 are based on those reported by Rempe et al. (1997).

For the base case, the heat transfer correlations listed in Table 1 are used. Fig. 6 shows the initial condition for the base case. The mean decay heat density is 2.1 MW/m^3 with an upper bound of about 3 MW/m^3 . The peculiar behavior of the uncertainty distribution

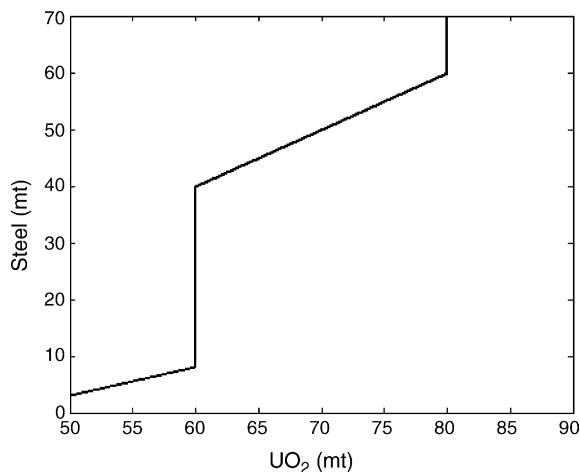


Fig. 5. Distribution of stainless steel in the lower plenum.

Table 4
Uncertainties in the emissivity of surfaces and the vessel thermal conductivity

Physical property	Mean	S.D.
Vessel thermal conductivity (W/m K)	32	2
Metal emissivity	0.29	0.04
Structure emissivity	0.8	0.03

for the steel mass shown in Fig. 6 is due to the dependence of the steel mass on the UO₂ mass relocation as was discussed earlier. Furthermore, the base case analyses assume a two-layer configuration of ceramic pool with an overlaying metallic layer (i.e., Configuration I).

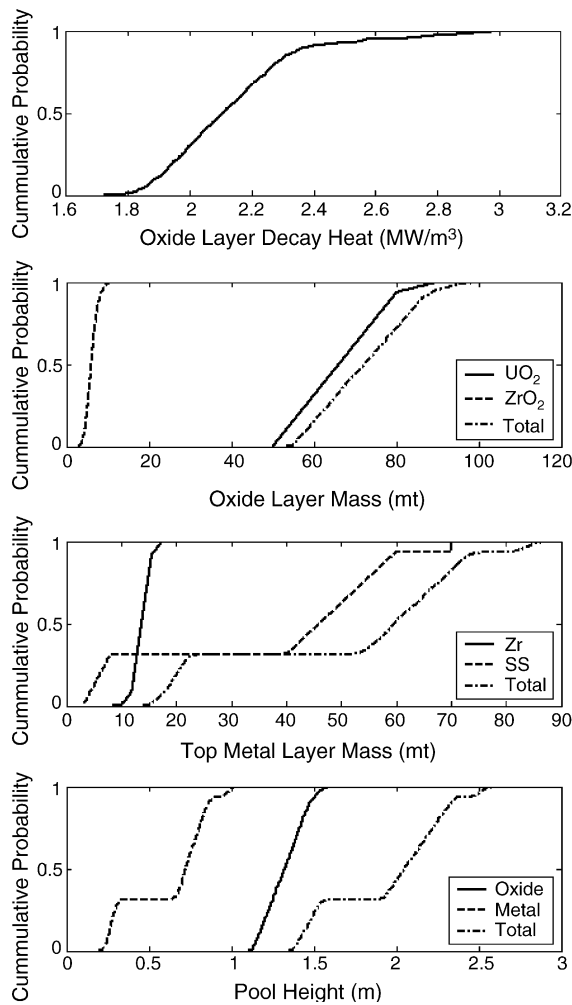


Fig. 6. Base case distribution of initial conditions.

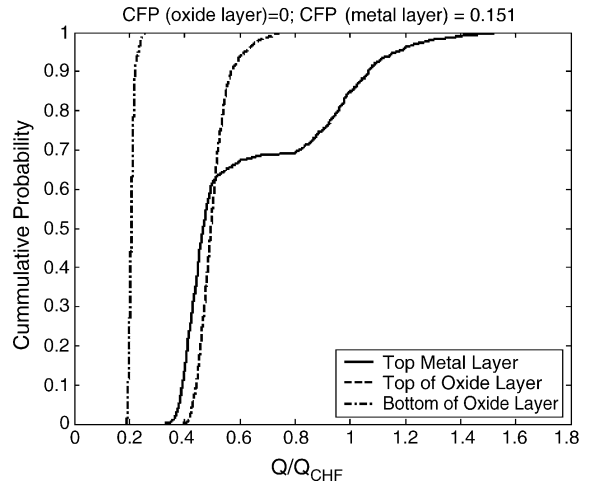


Fig. 7. Base case distributions of output parameters.

The ratio of the local heat flux to CHF is shown in Fig. 7. The distributions are shown at three locations: (1) at the bottom of the vessel; (2) at the top of the oxide layer adjacent to the metal layer; and (3) in the metal layer. Note that the height of the oxide layer varies with the mass of the debris in the lower plenum as shown in Fig. 6. Therefore, the top of the oxide layer is not at a fixed angle (the angle varies between 63° and 79° depending on the mass). However, since the maximum heat flux in the oxide layer occurs at the top, the distribution shown in Fig. 7 signifies the maximum heat flux. At the bottom of the vessel (at 0°), the heat flux is lowest, and even though the CHF is also lowest at this location, the ratio of q''/q''_{CHF} is around 0.2. At the top of the molten oxide layer, the heat flux ratio is significantly increased, but remains below 1. Therefore, the conditional failure probability is zero. In the metal layer; however, due to the focusing effect of the heat flux to the side of the vessel, the conditional failure probability is 0.15. The heat flux ratio can reach up to 1.5 in the upper bound. Significant melting of the vessel wall is predicted both in the top metallic layer region, and near the top of the molten oxide layer. No melting of the vessel wall is predicted at the bottom of the vessel.

Fig. 8 shows the distributions of the oxide layer crust thickness, the heat flux ratio to water, the heat flux ratio, and the vessel wall thickness as a function of the angle for a single realization of the input parameters. Fig. 8 uses the mean values of the parameter from

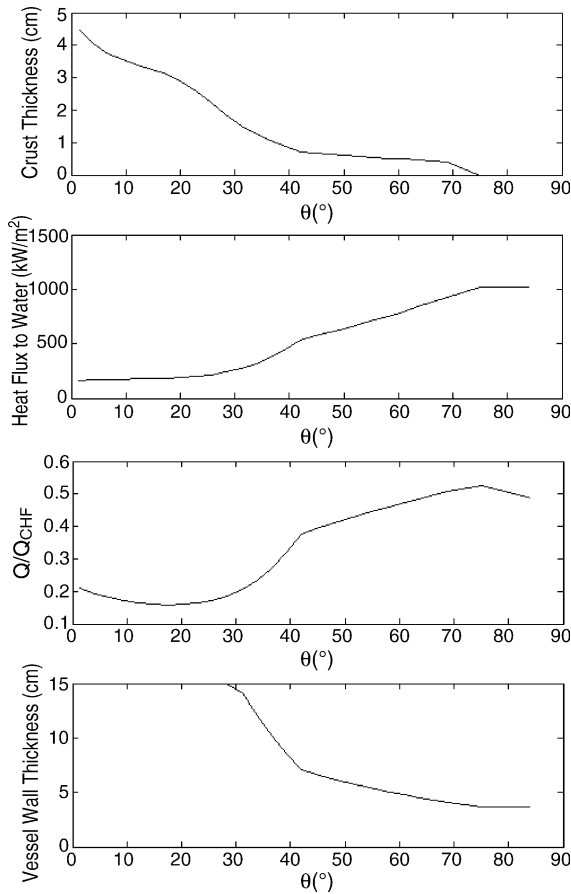


Fig. 8. Base case angular variation for mean values of parameters (Case 1).

various uncertainty distributions. This corresponds to 66,266 kg of UO_2 , 6211 kg of ZrO_2 , 13,714 kg of Zr, and 37,376 kg of steel. Fig. 9 uses the lower bound masses while the other parameters are the same as those used for the analysis of Fig. 8. The masses for Fig. 9 are 50,000 kg of UO_2 , 6307 kg of ZrO_2 , and 3000 kg of steel (note that there is no Zr in the light metal layer). Note that in the steel layer in Fig. 9, the heat flux to the cavity water is more than four times larger than the critical heat flux, which is due to the focusing effect of the top steel layer.

4.3. Sensitivity analysis (melt Configuration I)

A number of sensitivity calculations were performed to examine the impact of the initial conditions,

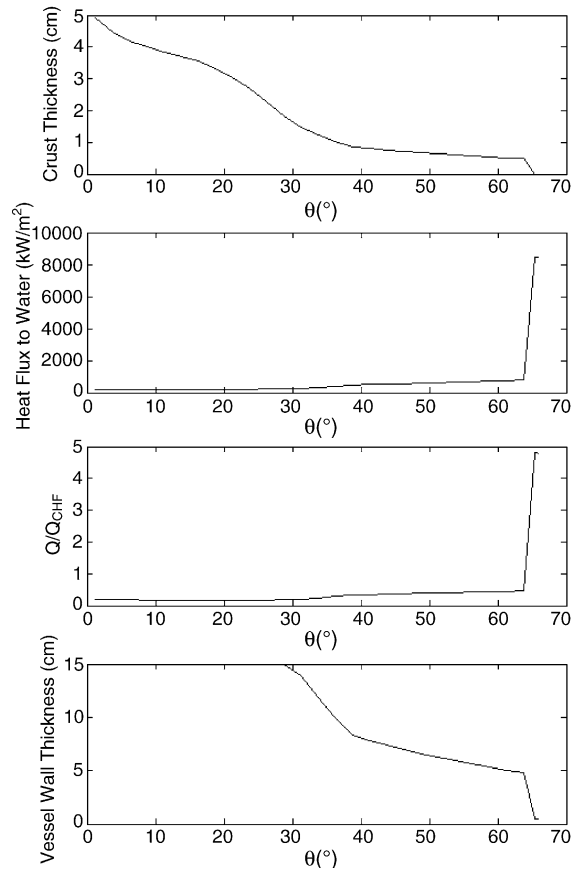


Fig. 9. Base case angular variation for low melt mass (Case 1).

and the heat transfer correlations on the conditional failure probability of the RPV lower head.

The list of the sensitivity calculations is given in Table 5. The largest impact on the conditional failure probability is due to the focusing effect associated with the low mass of debris in the lower plenum. The conditional failure probability is decreased by a factor of four from 0.15 to 0.04 for a reduction in the probability from 0.0193 to 0.0046 (see Fig. 4). For the case of the material properties in the sensitivity calculation, the point estimate mean values are used. The material properties distributions have minimal impact on the estimated conditional failure probability. The sensitivity case involving the heat transfer correlations shows that the conditional failure probability is within 30% of that using the base case correlations.

Table 5
Comparison of lower head conditional failure probabilities

Case	Description	Ceramic layer	Metal layer
In the absence of decay heat in the light metal layer			
1	Base case	0	0.15
2	Heat transfer correlations of Theofanous et al. (1996)	0	0.20
3	Heat transfer correlations of Rempe et al. (1997)	0	0.30
4	Material properties	0	0.16
5	Reduce probability of low UO ₂ mass	0	0.04
6	“Tails” of uncertainty distributions	0	0.16
7	Assumed $\pm 10\%$ uncertainty in CHF correlation	0	0.08–0.25
8	25% increase in heat transfer coefficient (oxide to light metal layer)	0	0.17
Including decay heat in the light metal layer			
1D	All other conditions identical to Case 1	0	0.27
2D	Heat transfer correlations of Theofanous et al. (1996)	0	0.30
3D	Heat transfer correlations of Rempe et al. (1997)	0	0.31
4D	Reduce probability of low UO ₂ mass	0	0.07
5D	“Tails” of uncertainty distributions	0	0.30
6D	Assumed $\pm 10\%$ uncertainty in CHF correlation	0	0.20–0.31
7D	25% increase in heat transfer coefficient (oxide to light metal layer)	0	0.29

For the decay heat in the top metal layer, the use of Eqs. (28) and the uncertainty distributions associated with Zr oxidation fraction and timing of release discussed earlier show that the fraction of the decay heat can vary between 0.1 and 0.2. In this series of sensitivity calculations (Cases 1D–7D), a normal distribution is assumed between the lower bound of 0.1 and the upper bound of 0.2 for the fraction of the decay heat in the top metal layer (the rest of the decay heat is in the oxide layer). The results show that a combination of the focusing effect and the additional power in the metal layer can increase the likelihood of failure by a factor of 2 for Case 1D, and 1.5 for Case 2D, respectively. However, for the case with the heat transfer correlations as used by Rempe et al. (1997) (Case 3D), there is no significant increase in the conditional failure probability (as compared with the same case without the decay heat in the metallic layer, i.e., Case 3). This result is not surprising, because for the case based on the correlations as used by Rempe et al. (1997) (Cases 3 and 3D), the fraction of upward heat transfer in the molten oxide pool is greater than for Cases 1 and 1D. At some point, increasing the decay power in the metal layer does not necessarily increase the conditional failure probability because of the reduction in the decay heat in the molten oxide pool. In fact, for Case 1D, if the upper bound of the decay heat fraction is increased from 0.2 to 0.9, there is only a modest increase from

0.27 to 0.32 in the estimated conditional failure probability.

In response to the peer review of the present study reference (Esmaili and Khatib-Rahbar, 2004), several additional sensitivity calculations were also performed. The first additional sensitivity involves the assessment of the impact of the tails of the uncertainty distributions on the conclusions of the IVR analysis (Cases 6 and 5D). This is not expected to change significantly the overall results of the IVR analysis. The input distributions are provided in Figs. 10–12. The tails of the uncertainty distributions associated with the initial conditions do not significantly affect the calculated results as shown in Table 5 and in Fig. 13. For the case without decay heat in the light metal layer, the failure probability increases from 0.15 (Case 1) to about 0.16 (Case 6), and for the case with decay heat in the top metallic layer, the lower head failure probability increases from 0.27 (1D) to 0.30 (5D).

The second additional sensitivity involves the assessment of the impact of the critical heat flux on the calculated lower head failure probability. This sensitivity calculation involves an arbitrary $\pm 10\%$ variation in the critical heat flux (i.e., Cases 7 and 6D), because the uncertainties associated with the measured critical heat flux have not been reported by Dinh et al. (2003). As indicated in Table 5, the uncertainties in the critical

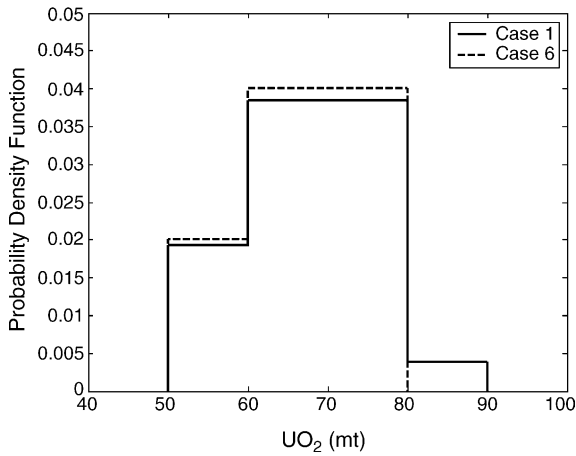


Fig. 10. Comparison of the distributions of UO_2 for AP1000 (Cases 1 and 6).

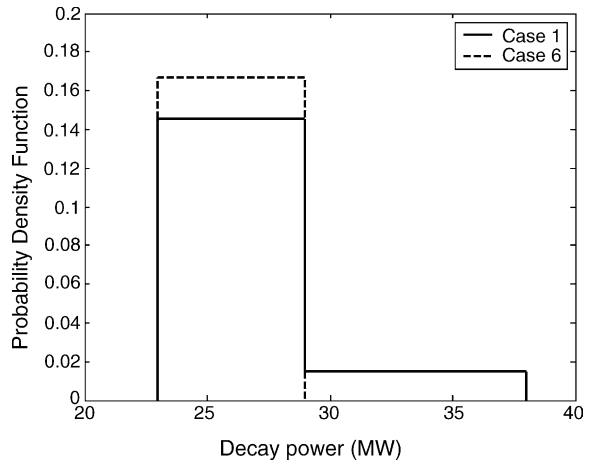


Fig. 12. Comparison of the distributions of decay power for AP1000 (Cases 1 and 6).

heat flux can have a significant impact on the calculated likelihood of lower head failure, which ranges from 0.08 to 0.25 for the case without any decay heat in the light metal layer (Case 7), and from 0.20 to 0.31 for the case that includes the contribution of decay heat in the light metal layer (Case 6D).

The third additional sensitivity involves the assessment of the impact of the heat transfer coefficient between the ceramic pool and the light metallic layer by arbitrarily increasing the existing Churchill and Chu (1975) heat transfer correlation by 25% (i.e., Cases

8 and 7D). The impact on the calculated conditional failure probability is minimal (see Table 5). The calculated failure probability increases from 0.15 (Case 1) to about 0.17 (Case 8) for the case without any decay heat, and from 0.27 (Case 1D) to about 0.29 (Case 7) for the case with decay heat in the light metallic layer, respectively.

The variations in the failure probabilities for these three cases are within the range of values for the other sensitivity cases as listed in Table 5. Therefore, the side failure of the lower head is likely.

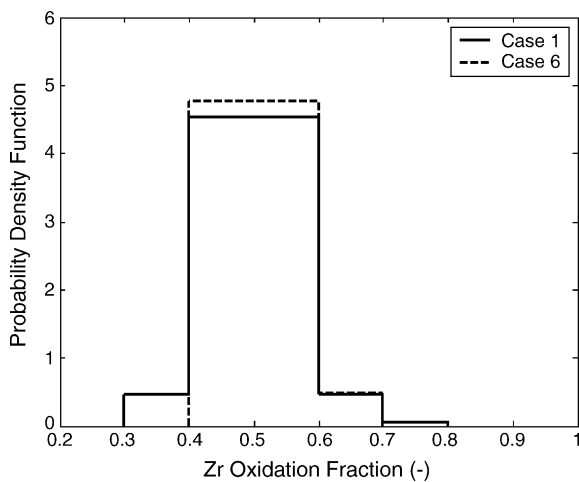


Fig. 11. Comparison of the distributions of Zr oxidation for AP1000 (Cases 1 and 6).

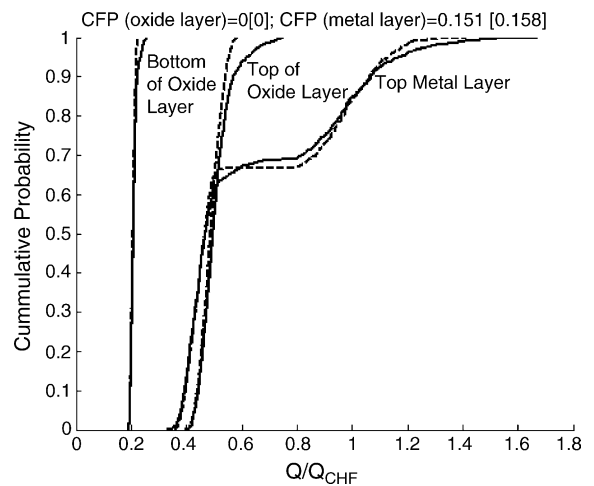


Fig. 13. Sensitivity to the initial conditions distributions for base case without decay heat in the light metal layer (Cases 1 and 6).

4.4. Melt Configuration II

Experiments performed at the Organization of Economic Cooperation and Development (OECD)-sponsored MASCA facility have shown the potential for partitioning of the major constituents (Zr, Fe, U) between oxide and metallic phases and the migration of metals through corium debris. This partitioning has also been studied at larger ratio of steel to corium mass content (Asmolov and Strizhov, 2004). The potential for heavier metallic melt partitioning has also been discussed by Powers and Behbahani (2004). Therefore, consistent with these observations, Configuration II involves a molten oxide layer between a heavier metal layer at the bottom, and a lighter metal layer at the top. It is important to recognize that the density of the bottom layer composed of U–Zr–SS must be greater than the density of the oxide layer. Since the density ratio is the limiting factor, it is only possible to perform parametric calculations for this configuration by ensuring that the density ratio is greater than 1 and the mass fraction of the uranium remains below the maximum 0.40. It should also be noted that there is no experimental database for the heat transfer in this configuration.

The parametric calculations involve point estimate mean values of the masses from Configuration I as discussed in the previous sections. For simplicity, the mass fraction of uranium is fixed at 0.4, and only the fraction of uranium is allowed to vary. The fraction of uranium that is in the oxide form (f_U) is defined as:

$$f_U = 1 - \frac{m_U}{M_{UO_2}} \frac{270}{238} \quad (30)$$

where M_{UO_2} is the total mass of UO_2 , and m_U the mass of uranium in the bottom layer. Therefore, the mass of U in the bottom heavy metal layer, and the mass of UO_2 in the ceramic layer are then given by:

$$m_U = [(1 - f_U)M_{UO_2}] \frac{238}{270}, \quad m_{UO_2} = f_U M_{UO_2} \quad (31)$$

The mass of ZrO_2 in the oxide layer is fixed, and the mass of steel in the bottom heavy metallic layer is only the lower plenum energy absorbers (3000 kg). Since the mass fraction of U is 0.40:

$$\frac{m_U}{m_{total}} = 0.40 \quad (32)$$

and

$$m_{total} = m_{Zr-bot} + m_{Fe} + m_U \quad (33)$$

Therefore, the mass of Zr in the bottom layer, and the mass of Zr in the top layer are given by:

$$m_{Zr-bot} = 1.5m_U - m_{Fe} = 1.5m_U - 3000 \quad (34)$$

$$m_{Zr-top} = M_{Zr} - m_{Zr-bot} \quad (35)$$

Table 6 shows the conditions for the parametric calculations, and the results of the calculations are shown in Table 7. It is seen that the calculation of the partitioning of the decay heat between the ceramic and the heavy metal pools using Eqs. (26) and (27) yield results that are very similar. The heat flux ratio for all the calculations is well below 1.

Therefore, in the absence of inter-metallic reactions, it appears that the lower head is not expected to fail at the bottom location, if partitioning of the heavy metals from the ceramic pool is conjectured. This conclusion is consistent to that of Scobel (2003).

4.5. Potential impact of inter-metallic reactions

The thermal interaction between the stratified light metal layer and the heavy metal layer that could form due to the partitioning of U–Zr–Fe in contact with the side and bottom portions of the reactor pressure vessel have been examined. These analyses showed that the thermal failure of the lower head due to the focusing effect of the stratified light metal layer is likely, while analysis results for the heavy metal layer showed that lower head failure at the RPV bottom location

Table 6
Melt quantities in each layer for Configuration II

Layer	U	UO_2	Zr	ZrO_2	Fe
Top metal (kg)	–	–	Eq. (32)	–	34366
Middle oxide (kg)	–	Eq. (31)	–	6211	–
Bottom metal (kg)	Eq. (31)	–	Eq. (32)	–	3000
Total (kg)	–	66266	13714	6211	37366

Table 7
Results of parametric calculations for Configuration II

f_U	0.95		0.9		0.85	
m_U (kg)	2921		5841		8762	
m_{UO_2} (kg)	62953		59639		56326	
ρ_h (kg/m ³)	8909		8584		8481	
ρ_o (kg/m ³)	8392		8377		8358	
V_h (m ³)	0.820		1.701		2.583	
$A_{h,b}$ (m ²)	4.69		6.86		8.56	
$\Delta h_{h,b}$ (m)	0.373		0.546		0.681	
V_o (m ³)	8.240		7.861		7.481	
Decay heat	Eq. (26)	Eq. (27)	Eq. (26)	Eq. (27)	Eq. (26)	Eq. (27)
Q_h (MW/m ³)	1.126	1.029	1.084	0.9915	1.071	0.978
Q_o (MW/m ³)	2.127	2.137	2.112	2.132	2.096	2.128
q''/q''_{CHF}	0.22	0.20	0.30	0.28	0.36	0.33

is not likely due to the significant margin to critical heat flux. However, these analyses did not consider the potential for inter-metallic reactions (Powers and Behbahani, 2004), including the reaction of molten Zr with the molten stainless steel resulting in significant heat generation, which at sufficiently high Zr mole fractions, can result in a self-propagating attack on the lower head.

In the light metallic layer, the Zr mole fraction is relatively smaller than that in the heavier bottom layer. Therefore, the impact of any self propagating mechanism for failure is not as significant, especially given the already high likelihood of failure due to thermal effects. Even in the bottom location, the additional steel that is ablated from the lower head due to any inter-metallic reactions, tends to mitigate this self-propagating effect (by reduction in the heat of mixing due to a reduction in the mole fraction of Zr in the mixture). Furthermore, the conditions that can result in the segregation of the heavy metals from the ceramic pools may not be sustainable (Asmolov and Strizhov, 2004). Consideration of the impact of inter-metallic reactions on the lower head integrity requires additional experimental and analytic studies.

5. Initial conditions for analysis of ex-vessel FCI loads

5.1. Melt initial conditions in the lower plenum

The quantification of molten debris mass, composition and temperature in the lower plenum at ves-

sel breach depends primarily on the accident scenario. The time scale for FCI is very short and would not involve the entire mass of the molten debris in the lower plenum. Based on the results of IVR analysis, the most likely failure of the RPV lower head is expected to occur in the light metallic layer due to the focusing effect that results in the local heat flux to exceed the critical heat flux. The best estimate melt temperature for the metallic layer is about 2060 K based on the results of the present IVR model.

5.2. Cavity condition at vessel breach

The AP1000 containment is designed to result in the submergence of the lower head in a very short time frame. Zavisca et al. (2003) also show that at the time of core relocation into the lower plenum, the depth of the water is sufficient to result in the full submergence of the RPV.

Furthermore, the results of calculations performed by Zavisca et al. (2003) also indicate that the containment pressure is about 2 bar and the cavity water is sub-cooled at a temperature of about 343 K following core relocation into the lower plenum. These calculations show that the cavity water remains sub-cooled for several hours following core relocation into the lower plenum.

5.3. Location, mode and size of vessel breach

The failure location impacts the dynamic pressures and the impulsive loads on the cavity wall and the reactor pressure vessel, especially if the failure location is

on the side of the vessel lower head and in the vicinity of the cavity wall. The best-estimate location of failure is on the side of the lower head in the light metallic region. The size of failure cannot be estimated with any degree of certainty. The results of the in-vessel retention analysis discussed previously show that the thickness of the metallic layer can be over 0.35 m before the critical heat flux is exceeded. Therefore, as a best estimate, a failure hole diameter of 0.4 m is assumed for the base case calculation. Using the upper bound values of 90 mt of UO_2 and decay heat of 38 MW, the metallic melt layer thickness can be as high as 0.53 m before the critical heat flux is exceeded. Therefore, a sensitivity to a larger hole size of 0.6 m is also considered. Furthermore, to assess the potential impact of RPV failure at the bottom location (e.g., due to materials interactions effects), a sensitivity case that involves RPV failure at the bottom of the reactor pressure vessel (assuming a failure size of 0.4 m) is also considered.

6. Results of analysis of ex-vessel FCI energetics

In the present study, the FCI processes are modeled using the two-dimensional PM-ALPHA (Yuen and Theofanous, 1995) and ESPROSE.m (Theofanous and Yuen, 1995) computer codes.

The RPV is modeled as an “obstacle” in the computation domain. Fig. 14 shows the problem nodalization, the representation of the hemispherical lower head with a number of horizontal and vertical lines, signifying the presence of the obstacles. Only a narrow annular region of thickness 0.4 m is available for the propagation of the explosion around the cylindrical portion of the RPV.

The insulation that surrounds the RPV lower head may potentially affect the fuel coolant mixing process and the subsequent explosion propagation/expansion. The presence of the insulation may have two important effects. During the mixing phase, the insulation could alter the flow of the molten material and prevent efficient fuel coolant mixing. It would restrict the amount of water that could mix with the fuel and actually increase the void fraction of the vapor present in the region near the vessel wall. In addition, after the metallic melt has melted through the insulation, the residual passages in the insulation could trap vapor and provide a certain degree of compliance to the rigid boundary of the RPV outer wall. These two ef-

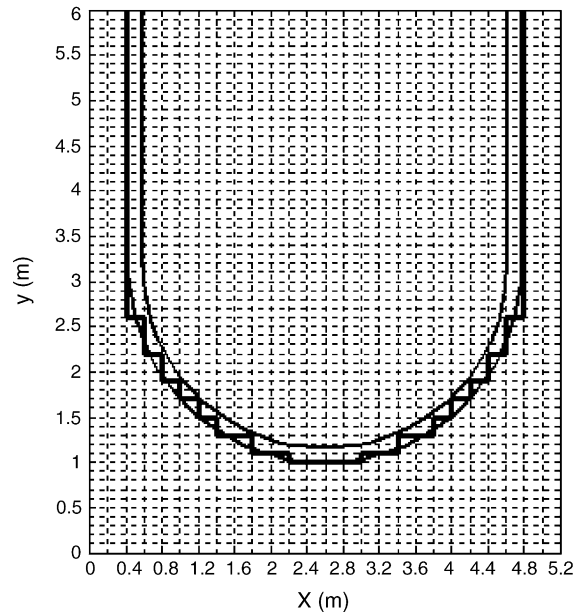


Fig. 14. Schematic of lower head nodalization.

fects of altering the mixing process and providing a larger degree of “boundary compliance” to the RPV wall could diminish the focusing effects of this surface and thereby reduce the dynamic pressures in the local region. However, it is difficult to quantify the impact of the thermal insulation on the dynamic pressure using the available computer codes, especially in light of the uncertainties that are inherent in the fuel coolant interaction phenomena.

For the PM-ALPHA calculation, the melt inlet location is about 2 m above the cavity floor; therefore, the size of the computational domain is 2 m in the vertical direction (20 nodes) and 3 m in the horizontal direction (15 nodes). The last node in the vertical direction represents a steam gap. PM-ALPHA requires the inlet to be at the boundaries of the computational domain, and does not accept an inlet below the surface of the water pool. The PM-ALPHA calculation is only performed to obtain the conditions for the ESPROSE.m explosion propagation simulation. The entire RPV including the cylindrical portion up to a distance of 6 m from the cavity floor is modeled as an obstacle. An additional 1 m of steam gap is also included to allow for the venting of the explosion. The water pool depth of 5 m is modeled that is consistent with the results of Zavisca et al. (2003).

6.1. Base case

The base case calculations used a metallic pour re-locating through a lower head failure size of 0.4 m in diameter at 2060 K into the cavity water at 343 K. The pour velocity is 1.7 m/s, and the melt particle diameter is 0.01 m assuming a maximum fragmentation rate per particle of 4 kg/s.

The initial distribution of the melt volume fraction based on the ESPROSE.m premixing calculation is shown in Fig. 15. The water pool sub-cooling leads to suppression of the vapor void fraction. These conditions are conducive to high pressurization. The duration of the premixing was 1 s to allow the melt to reach the cavity floor before the explosion is triggered.

The propagation of the pressure in the cavity around the RPV is shown at different times in Figs. 16–18 (the pressure is in MPa). The water sub-cooling leads to high pressures in the explosion zone. However, the pressure venting from the top of the water pool around the gap ultimately leads to a reduction in pressure in the water pool.

The explosion is triggered at the bottom of the vessel, and it takes about 1 ms for the pressure to propagate to the lower head. By 2 ms, the pressure in the pool reaches about 80 MPa, and the wave is propagating downward toward the cavity floor and away from the explosion zone. At 6 ms, the pressure wave has already

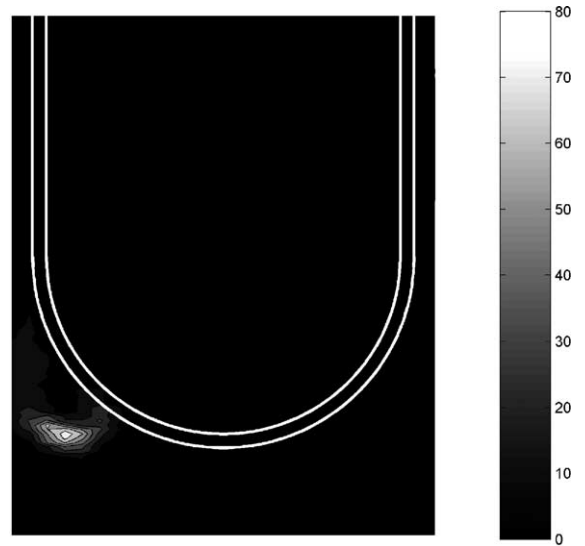


Fig. 16. Predicted pressure distribution (in MPa) in the cavity at 2 ms.

reached the cavity wall away from the explosion zone. The maximum pressure in the cavity pool, and the pressures on the cavity wall are shown in Figs. 19 and 20. The maximum impulse load on the cavity wall is about 85 kPa s as shown in Fig. 21. It should be noted that this calculations was run for 6 ms. It is clear from the maximum pressure in the pool that by this time, the explosion is slowly dissipating. The pressure traces on the

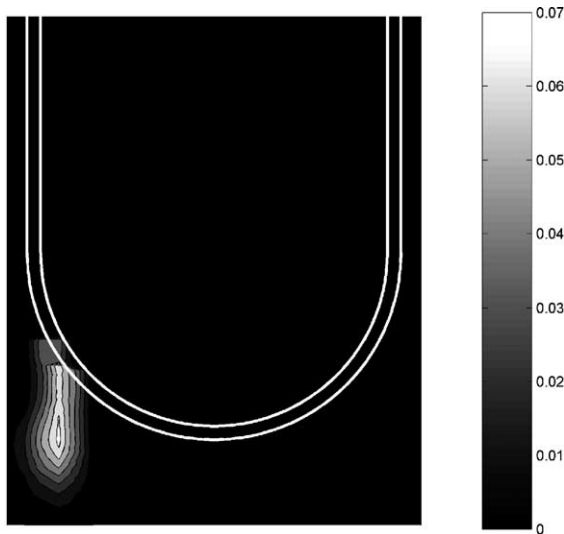


Fig. 15. Melt volume fraction at the end of mixing calculation.

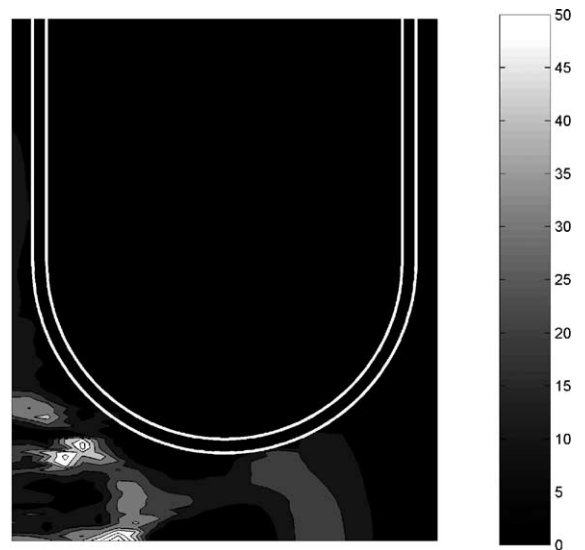


Fig. 17. Predicted pressure distribution (in MPa) in the cavity at 4 ms.

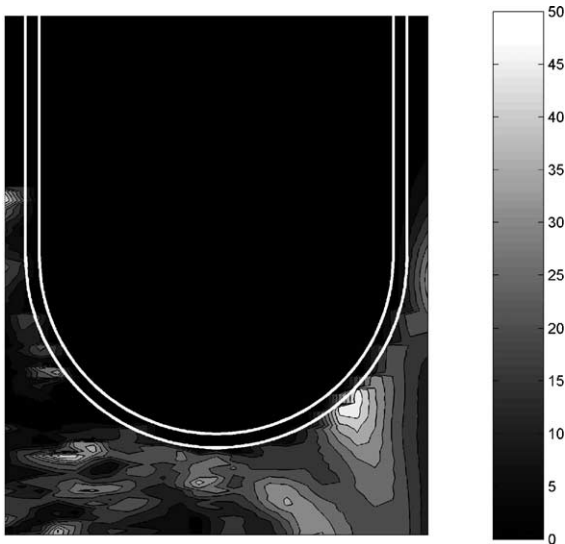


Fig. 18. Predicted pressure distribution (in MPa) in the cavity at 6 ms.

cavity wall at different axial locations show a complicated pattern of multiple reflections and pressure peaks as a result of interaction with the RPV lower head structure.

6.2. Sensitivity calculations

The choice of the sensitivity calculations is based on the results of the AP600 fuel coolant interaction calculations (Khatib-Rahbar et al., 1996) that showed greater sensitivity to certain initial conditions and model pa-

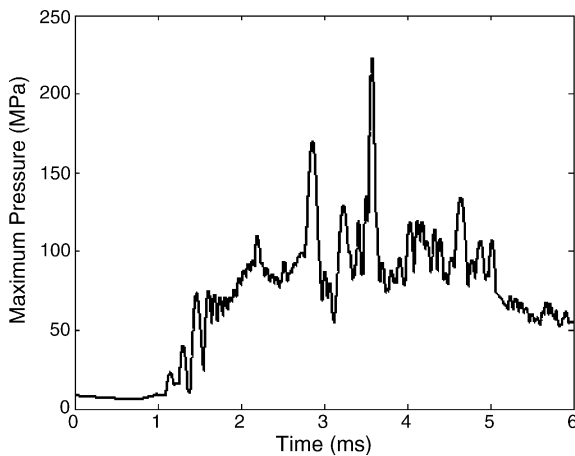


Fig. 19. Predicted maximum pressure in the cavity water pool.

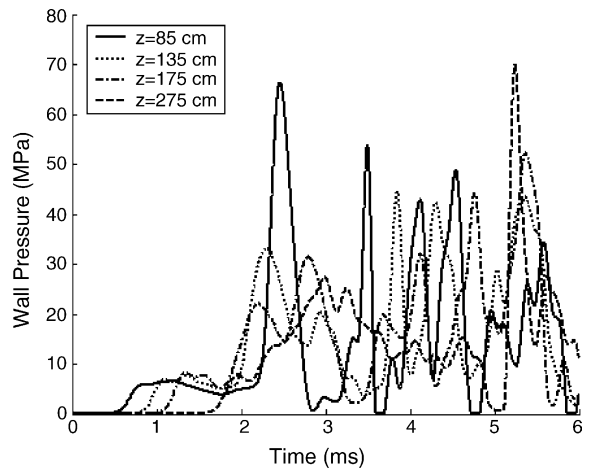


Fig. 20. Predicted cavity wall pressures at various axial locations.

rameters. The differences between AP600 and AP1000 that could possibly affect the explosion energetics are the smaller distance between the bottom of the vessel and the cavity floor in AP1000, and the initial melt pour velocity. Due to the closer proximity of the RPV from the cavity floor, and because the explosion is triggered when the melt reaches the cavity floor, the initial condition for the calculations would involve a lower melt mass (as compared with AP600) participating in the explosion. In addition, the initial melt pour velocity in AP600 (Khatib-Rahbar et al., 1996) was estimated to be 2.9 m/s, whereas for the present AP1000 study,

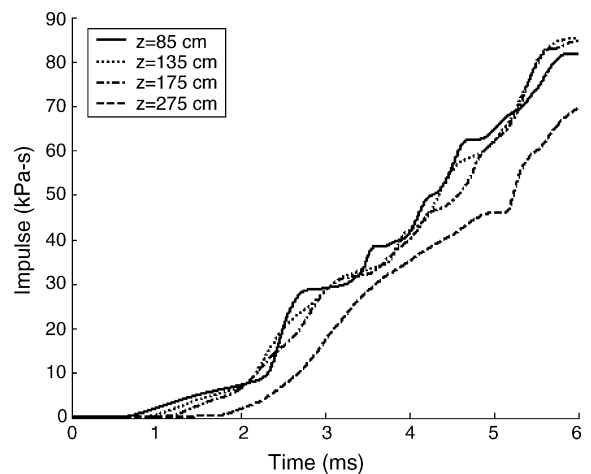


Fig. 21. Predicted cavity wall impulse loads at various axial locations.

Table 8
Summary of the maximum loads resulting from energetic FCIs

Case	Impulse load (kPa s)	Wall pressure (MPa)	Maximum pool pressure (MPa)
Base case	85	90	220
Ceramic melt (at 3150 K)	305	290	1000
Hole diameter of 0.6 m	145	135	425
Particle diameter of 0.1 m and maximum fragmentation rate of 400 kg/s per particle	12	8	10
Bottom failure of the lower head	9	8	60

the velocity is 1.7 m/s. Since the pour rate is directly proportional to the velocity, the AP1000 pour rate is estimated to be lower than AP600. Overall, these differences are expected to result in lower pressurization and impulse loading on the cavity wall for AP1000 as compared to the results for AP600 (Khatib-Rahbar et al., 1996).

The results of the sensitivity calculations are shown in Table 8. The composition of the melt has a significant impact on the calculated impulse loads on the cavity wall. The ceramic melt has a higher thermal energy and density as compared with the metallic melt. These tend to increase the rate of fragmentation during the escalation and propagation phase of the explosion, and thereby, cause an increase in the maximum explosion pressures and the impulse loads.

It should be mentioned that the present study does not consider the effects of chemical energy augmentation due to the presence of large metallic constituents. Chemical energy augmentation could have a significant impact on the dynamics of the explosion. Increasing the RPV failure size, and thus the quantity of the melt pour into the cavity water pool, increases the local pressures and the impulse loads on the cavity wall. Uncertainties in the fragmentation model parameters have a considerable impact on the energetics of fuel coolant interactions. In ESPROSE.m, the particle diameter and the maximum rate of fragmentation per particle can substantially impact the predicted pressures and the impulse loads. Increasing the assumed initial particle diameter from 0.01 m in the base case to 0.1 m, and the maximum fragmentation rate from 4 kg/s to 400 kg/s per particle, the maximum predicted impulse load was 12 kPa s compared with 85 kPa s for the base case. For the bottom failure of the lower head, the amount of melt in the pool before the explosion is triggered is limited due to the proximity of the lower head to the

cavity floor. For the case of the ceramic melt with a high melt superheat, the earlier analysis for AP600 using the same methods resulted in an impulse load on the cavity wall that was a factor of 2 larger than that listed in Table 8 (i.e., in the range of 600–700 kPa s for AP600 that was found to be below the expected structural capacity of the cavity and containment (USNRC, 1998)). The result of the present calculations show that the expected impulse loads on the AP1000 cavity wall and RPV structures are benign when compared to those for AP600 (Esmaili and Khatib-Rahbar, 2004), which were found to be inconsequential by USNRC (1998).

7. Conclusions

The results of the base case calculation for melt Configuration I showed that the local heat flux in the light overlaying metallic layer exceeded the critical heat flux due to the focusing effect associated with the presence of thin stratified metallic layers. The presence of thin stratified metallic layers overlaying the ceramic pool cannot be ruled out due to the uncertainties in late phase melt progression. On the other hand, it was found that the local heat flux always remained below the critical heat flux limit in the molten ceramic region. Parametric sensitivity calculations covering a wide range of uncertainties associated with melt Configuration I showed that the lower head failure probability can range from ~ 0.04 to ~ 0.3 depending on the likelihood that is assigned to the initial melt relocations that would involve smaller quantities of ceramic material into the lower plenum, and the heat transfer correlations that are used in the calculations.

On the other hand, the results of the parametric calculations for melt Configuration II showed that the heat flux remained well below the critical heat flux,

rendering the thermal failure of the lower head at the bottom location improbable.

Notwithstanding the uncertainties in the underlying phenomena associated with the fuel coolant interaction, based on two-dimensional computer code calculations, it was shown that there is a potential for large impulse loads on the cavity and the RPV structures (and subsequently the containment penetrations) in the AP1000. However, the calculated impulse loads on the cavity wall for AP1000 were found to be below those estimated for AP600 using a similar approach.

Acknowledgements

The authors acknowledge valuable peer review comments by Drs. M.L. Corradini (University of Wisconsin-Madison), V.K. Dhir (University of California, Los Angeles) and F. Moody (Consultant, formerly of General Electric Company). This work was performed under the auspices of U.S. Nuclear Regulatory Commission, Office of Nuclear Regulatory Research, Contract Number NRC-RES-04-02-075.

References

- Allison, C.M., Rempe, J.L., Chavez, S.A., 1994. Design report on SCDAP/RELAP5 model improvements—debris bed and molten pool behavior. INEEL-94/0174.
- Asfia, F.J., Dhir, V.K., 1996. An experimental study of natural convection in a volumetrically heated spherical pool bounded on top with a rigid wall. *Nucl. Eng. Design* 163, 333–348.
- Asmolov, V., Strizhov, V., 2004. Overview of the progress in the OECD MASCA project. In: Proceedings of the Cooperative Severe Accident Research Program (CSARP) Meeting, Marriott Crystal Gateway, May 3–4.
- Churchill, S.W., Chu, H.H.S., 1975. Correlating equations for laminar and turbulent free convection from a vertical plate. *Int. J. Heat Mass Transfer* 18, 1323.
- Dinh, T.N., Tu, T.P., Salmassi, T., Theofanous, T.G., 2003. Limits of coolability in the AP1000-related ULPU-2400 Configuration V facility. In: Proceedings of the 10th International Topical Meeting on Nuclear Reactor Thermal Hydraulics (NURETH-10), Seoul, Korea, October 5–9.
- Esmaili, H., Ali, S., Vijaykumar, R., Khatib-Rahbar, M., 1996. Evaluation of debris coolability by external cooling of the lower head for AP600 using MELCOR. Energy Research, Inc., ERI/NRC 96-201.
- Esmaili, H., Khatib-Rahbar, M., 2004. Analysis of in-vessel retention and ex-vessel fuel coolant interaction for AP1000. Energy Research, Inc., ERI/NRC 04-201, NUREG/CR-6849.
- Globe, S., Dropkin, D., 1959. Natural convection heat transfer in liquid confined by two horizontal plates and heated from below. *Trans. ASME* 81C, 24.
- Henry, R., Fauske, H., 1993. External cooling of a reactor vessel under severe accident conditions. *Nucl. Eng. Design* 139, 31–43.
- Iman, R.L., Shortencarier, M.J., 1984. A FORTRAN 77 program and user's guide for the generation of Latin hypercube and random samples for use with computer models. NUREG/CR-3624.
- Khatib-Rahbar, M., Esmaili, H., Vijaykumar, R., Wagage, H., 1996. An assessment of ex-vessel steam explosions in the AP600 advanced pressurized water reactor. Energy Research, Inc., ERI/NRC 95-211.
- Kulacki, F.A., Emara, A.A., 1975. High Rayleigh number convection in enclosed fluid layers with internal heat sources. USNRC, NUREG-75/065.
- Kymfilfiinen, O., Tuomisto, H., Theofanous, T.G., 1997. In-vessel retention of corium at the Loviisa plant. *Nucl. Eng. Design* 169, 109–130.
- Mayinger, F., et al., 1976. Examination of thermohydraulic processes and heat transfer in a core melt. BMFT RS 48/1, Institute für Verfahrenstechnik der TU, Hanover, Germany.
- O'Brien, J.E., Hawkes, G.L., 1991. Thermal analysis of a reactor lower head with core relocation and external boiling heat transfer. *AIChE Symp. Ser.* 87 283, 159–168.
- Park, H., Dhir, V.K., 1991. Steady state analysis of external cooling of a PWR vessel lower head. *AIChE Symp. Ser.* 87 283, 1–12.
- Park, H., Dhir, V.K., 1992. Effect of outside cooling on the thermal behavior of a pressurized water reactor vessel lower head. *Nucl. Technol.* 100, 331.
- Pilch, M.M., et al., 1996. Resolution of the direct containment heating issue for all Westinghouse plants with large dry containments or sub-atmospheric containments. NUREG/CR-6338.
- Powers, D., Behbahani, A., 2004. Density stratification of core debris. In: Proceedings of the OECD MASCA Seminar, Paris, France.
- Rempe, J.L., et al., 1997. Potential for AP600 in-vessel retention through ex-vessel flooding. Technical Evaluation Report, INEEL/EXT-97-00779.
- Rohsenow, W.M., 1952. A method of correlating heat transfer data for surface boiling of liquids. *Trans. ASME* 74, 969.
- Scobel, J.H., 2003. The potential for AP1000 reactor vessel failure induced by a stratified debris bed with a bottom metal layer during IVR. In: Proceedings of the 2003 International Congress on Advances in Nuclear Power Plants, Córdoba, Spain.
- Sehgal, B.R., et al., 2003. Assessment of reactor vessel integrity (ARVI). *Nucl. Eng. Design* 221, 23–53.
- Seiler, J.M., et al., 2003. Analysis of corium recovery concepts by the EUROCORE Group. *Nucl. Eng. Design* 221, 119–136.
- Theofanous, T.G., et al., 1994a. Critical heat flux through curved, downwards facing thick wall. In: Proceedings of the OECD/CSNI/NEA Workshop on Large Molten Pool Heat Transfer, Gernoble, France.
- Theofanous, T.G., et al., 1994b. Experience from the first two integrated approaches to in-vessel retention through external cooling. In: Proceedings of the OECD/CSNI/NEA Workshop on Large Molten Pool Heat Transfer, Gernoble, France.

- Theofanous, T.G., Yuen, W.W., 1995. ESPROSE.m: A computer code for addressing the escalation/propagation of steam explosions. DOE/ID-10501.
- Theofanous, T.G., et al., 1996. In-vessel coolability and retention of a core melt. DOE/ID-10460, vol. I.
- Theofanous, T.G., Angelini, S., 2000. Natural convection for in-vessel retention at prototypic Rayleigh numbers. *Nucl. Eng. Design* 200, 1–9.
- Turland, B.D., Morgan, J., 1983. Thermal attack of core debris on a PWR reactor vessel. In: *Proceedings of the International Meeting on Light Water Reactor Severe Accident Evaluation*, Cambridge, MA, August 28–September 1.
- Turland, B.D., 1994. In-vessel phenomena relevant to the achievement of debris coolability by ex-vessel flooding for a PWR. In: *Proceedings of the OECD/CSNI/NEA Workshop on Large Molten Pool Heat Transfer*, Grenoble, France.
- United States Nuclear Regulatory Commission (USNRC), 1998. AP600 final safety evaluation report related to the certification of the AP600 design. NUREG-1512.
- Young, M.F., 1982. The TEXAS code for fuel–coolant interaction analysis. In: *Proceedings of ANS/ENS LMFBR Safety Topical Meeting*, Lyon-Ecully, France.
- Yuan, Z., Zavisca, M., Khatib-Rahbar, M., 2003. Impact of the reactor pressure vessel insulation on the progression of severe accidents in AP1000. Energy Research, Inc., ERI/NRC 03-205.
- Yuen, W.W., Theofanous, T.G., 1995. PM-ALPHA: a computer code for addressing the premixing of steam explosions. DOE/ID-10502.
- Zavisca, M., Yuan, Z., Khatib-Rahbar, M., 2003. Analysis of selected accident scenarios for AP1000. Energy Research, Inc., ERI/NRC 03-201.